thermo

MDPI

Article

A Quasi-Dimensional Model of Heat Transfer between Multi-Concentric Monolith Structures

Seamus P. Kane and William F. Northrop *

Department of Mechanical Engineering, University of Minnesota, Minneapolis, MN 55455, USA; kane0308@umn.edu

* Correspondence: wnorthro@umn.edu; Tel.: +1-612-625-6854

Abstract: Metallic monolith structures are often used in compact reactor applications due to their superior heat transfer properties and lower pressure drop when compared to ceramic monoliths. Endothermic reactions like steam reforming depend heavily on externally supplied heat, making highly conductive supports especially useful. Simulations are invaluable for designing effective reactors with complex catalyst support structures but are conventionally resource-intensive. Additionally, few dedicated heat transfer experiments between monoliths exist in prior literature. To expand general knowledge of heat transfer between metal monolith structures, this work investigated heat exchange in concentric monoliths brazed to a common mantle. A computationally inexpensive quasi-dimensional model was developed and used to predict the heat exchange effectiveness and intrinsic heat transfer rate. The model used a discretized control volume approach and simplified geometries to reduce computational intensity. The model was calibrated against experimental data collected using a steady-state flow bench. After calibration, a parametric study was performed where monolith construction and flow conditions were varied. A parametric analysis showed that for identical catalyst space velocities and volumes, heat exchange effectiveness can be increased by 43.2% and heat transfer rates by 44.8% simply through increasing the surface area to volume ratio of the monolith. The described approach serves as an alternative framework for modeling catalytic heat exchangers without heavy computation and for quickly matching monolith geometries to their intended use and operating range.

Keywords: metal monolith; heat transfer; catalysts; modeling; parametric study

Citation: Kane, S.P.; Northrop, W.F. A Quasi-Dimensional Model of Heat Transfer between Multi-Concentric Monolith Structures. *Thermo* **2023**, *3*, 515–536. https://doi.org/10.3390/thermo3040031

Academic Editor: Marcello Iasiello

Received: 4 August 2023
Revised: 11 September 2023
Accepted: 18 September 2023
Published: 26 September 2023

1. Introduction

Monolithic honeycomb structures are used extensively as supports in catalytic processes, especially in internal combustion engine exhaust aftertreatment applications [1,2]. Tubular monoliths possess higher open facial areas and greater mechanical strength relative to conventional pellets or packed beds. These features also allow high specific surface areas, low differential pressure, and relatively homogeneous thermal conditions even at high throughput [3–7]. The open structure of monoliths also decreases weight and thermal mass relative to pellet media, which is important in mobile applications where both rapid heating and light-off improve conversion efficiency during transient operation. Ceramic monoliths are more commonly used than metallic types for automotive applications due to easier wash-coat adhesion [6]. Despite this, corrugated metal monoliths offer thermal and design benefits, which may outweigh their disadvantages.

Metallic monolith performance surpasses that of ceramics in several ways. Thin foils used in their construction increase the open area, decreasing the pressure drop [8] and weight, while maintaining a mechanically robust structure. Metals are more thermally conductive than ceramics, which decreases thermal stratification in the reactor [6,9]. Finally, metal monoliths can be formed using rolling techniques, which offer additional geometries not available through extrusion [10]. Monolith cell profiles can be sinusoidal, square,

or triangular, each of which offers unique flow characteristics. Exceptionally small cell densities are possible, which creates large specific surfaces area for high catalyst loading. Open-cell monoliths, which behave like metal foams, can be built using perforated sheet stock [10,11], offering inter-channel flow mixing at a relatively lower cost. These thermal and fluid factors offer additional degrees of freedom in catalyst manufacturing not available to conventional ceramics. Full comprehension of these factors is of great value and will inform the next generation of novel catalytic technologies.

Previous work in monolith catalyst heat transfer modeling has primarily taken two approaches. One approach is to resolve an individual channel of the monolith in high detail, capturing turbulence and thermal stratification throughout. Heat transfer between channels is then inferred by expanding the single channel result to the full scale of the reactor. Studies by Cornejo et al. [12,13] examined the heat transfer effects within single cells of metallic monoliths. Their investigations used computational fluid dynamics (CFD) to investigate the relation between the Nusselt number (Nu) and the flow characteristics in the channel. CFD is more computationally cost effective when used to resolve smaller portions of a larger system.

The second approach to model monolith heat transfer is to consider the entire reactor using CFD or quasi-dimensional simulations without resolving individual channels. For example, an automotive catalytic converter was modeled by Hayes et al. [14] using CFD and 2D symmetry approximation. This model could solve simple flow cases in a matter of seconds; however, simulating catalyst light-off took up to 2 h. Modeling the entire reactor can be computationally less expensive under certain conditions but loses some of the finer physics and chemistry present at the channel level. This tradeoff is well illustrated by Sadeghi et al. [15], where the same reactor conditions are modeled using increasing dimensionality and different mathematical approaches. Despite modeling the same conditions, adding dimensions to the approach changed nitric oxide (NO) concentration and conversion rates over the length of the reactor. In this work, we present a quasi-dimensional modeling approach of the second variety, where the whole heat exchanger was resolved using quasi-dimensional methods. At the same time, our approach resolved cellular channel effects using geometric and thermal assumptions developed in prior works for single channel analyses. The net benefit of this approach is a computationally lean model, which still resolves dimensional stratification of the entire reactor.

Although comprehensive studies are sparse, metal monolith heat transfer has been of interest for many decades. An early foundational study by R.K. Shah [16] developed an initial understanding of thermal transfer in arbitrary shaped ducts. Here, steady-state Nusselt number (Nu) values were determined for developed laminar flow in numerous duct geometries. These Nu values are critical for monolith models, as Nu is a constant, and can be applied to every repeated tubular cell in the monolith. Simple models can be developed using accurate estimation of gas properties and proper selection of Nu. While fully developed Nu values differ in the literature for different cellular profiles, the constant and uniform Nu assumption can apply to a fixed profile and greatly simplifies modeling. For metal monoliths where the channel hydraulic diameter (D_h) is much smaller than their length ($D_h << L$), this assumption is accurate.

A later study by Boger and Heibel [17] calculated the apparent convective heat transfer coefficients in copper, aluminum, and cordierite monoliths. Heated gas was flowed through the samples, which were cooled with a circulating water jacket. Results showed apparent heat transfer coefficients of 1000 W/m^2K or greater in metallic monoliths, which exceeded that of cordierite by an order of magnitude. They concluded that monolith thermal conductivity caused the higher measured heat transfer rates. Similar apparent rates were measured in a reactor study by Roh et al. [18] using coated FeCrAl foil monoliths. The FeCrAl monolith demonstrated superior heat exchange when compared to a packed bed reactor operating under identical temperatures and flows.

More recent modeling studies have also explored coupling of dissimilar monoliths in both CFD and using genetic algorithm optimization. Regarding Cornejo et al. [19] and

Reinao et al. [20], the use of concentric cylinder/ring paired monoliths with a single inflow of reactants was showed to affect catalyst conversion. The variation and fine-tuning of the relative fraction of the cylinder to ring can distribute heat optimally for a reaction. Regarding Cherif et al. [21], application of a cheaper base-metal catalyst and conversion of methane within a cylindrical bed was optimized through a genetic algorithm approach. Careful sizing of concentric ring sections and varying catalyst type can create a more thermally uniform reactor, which performs similarly to a catalyst bearing only platinum materials. Together, these recent works demonstrate the importance of understanding concentric monolith heat exchange and the value of an increasing number of modeling procedures available for its study.

Catalyst substrate selection also has an important role in heat exchange within a reactor. Highly endothermic reactors such as steam reformers require high heating rates to maintain efficient conversion. Understanding and enhancing heat exchange allows both efficient operation and reactor intensification. This is especially crucial for waste-heat-driven compact reforming due to lower possible temperature differentials than in electrically heated or flame-heated reactors. For example, compact methane steam reforming (MSR) was achieved by Tonkovich et al. [22] at temperatures near 850 °C. In contrast, normal waste heat temperatures available from diesel engines and turbines are only 600 °C [23] and 650 °C [24], respectively. The importance of support thermal conductivity was demonstrated in a study by Ryu et al. [25], where a metallic monolith increased conversion and activity of MSR over that of a powdered catalyst bed. The metal monolith reactor also achieved this conversion while using only 18% of the powdered catalyst metal loading, significantly reducing the cost of such a reactor.

In this work, heat exchange between two metal monoliths brazed to a shared central mantle was experimentally measured and then modeled using a quasi-dimensional approach. Once model–experimental agreement was established, the model was then used to parametrically investigate heat exchange behavior of monoliths under varied thermal and physical constraints and determine the effects of each on the heat exchange rate and efficiency. The model is more computationally efficient than previous multi-dimensional approaches while providing dimensional insights not found in correlations and simpler models. Through its speed and general applicability, the developed approach expedites the design and construction process of experimental metal monolith reactors that include heat transfer by design. Furthermore, the model can be re-calibrated when new experimental data are available, increasing specificity and accuracy. By retaining only essential thermal and physical properties in a quasi-dimensional model, this work demonstrates a dimensionally resolved yet fast method for modeling thermal behavior in a metallic monolith reactor.

2. Quasi-Dimensional Modeling Method

2.1. Discrete Control-Volume Approach

Most monolith substrates can be approximated simply as a tube bundle. Tube diameters are equal and repeat in a measurable pattern. The tubes can exchange heat through their shared walls; a process driven primarily by convective effects. The quasi-2D model presented in this work assumes the monolith can be approximated as an assembly of identical ducts for which temperature varies primarily in the axial and radial direction. Heat and mass transfer effects were closely approximated using finite difference methods and were adapted from literature examples of quasi-2D reactor modeling [26,27]. Ducts were modeled as discrete control volumes, and solved simultaneously in the radial direction, then sequentially in the axial direction using a finite difference approach and conservation laws. Model continuity is given with Equation (1), where N_s is the number of constituent species in the gas mixture. Energy conservation is given with Equation (2) and accounts for the heat exchange in and out of the control volume in the radial direction. The total wall thermal resistance (R_{th}) was formulated to include the convective conditions on both sides, the conductive resistance through the wall, and a parallel conduction term for the

solid monolith foil. An increasing number of axial divisions was used to minimize the error generated using the finite difference approach, with the final division count determined with model convergence.

$$\left(\sum_{j=1}^{N_s} \dot{n}_j M_j\right)_i = \left(\sum_{j=1}^{N_s} \dot{n}_j M_j\right)_{i+1} \tag{1}$$

$$\frac{dT}{dt} = \frac{1}{\dot{m} c_p}\left[(T_i - T_{i-1})\frac{2r_i dx}{R_{th,i}} - (T_{i+1} - T_i)\frac{2r_{i+1} dx}{R_{th,i+1}}\right] \tag{2}$$

Heat is assumed to flow only in the radial direction, perpendicular to the corrugations. Axial thermal gradients were thus caused by radial heat transfer coupled with sequential axial solving of discrete parcels. Radial symmetry was also assumed to reduce modeling complexity. Actual metal monolith corrugations are arranged in a continuous spiral, which would break the radial symmetry assumption. However, modeled corrugations are very small, so this effect was assumed to be negligible on average across the whole monolith. This symmetry assumption is illustrated in the rectangular coordinates given in Figure 1 but holds conceptually for cylindrical geometries.

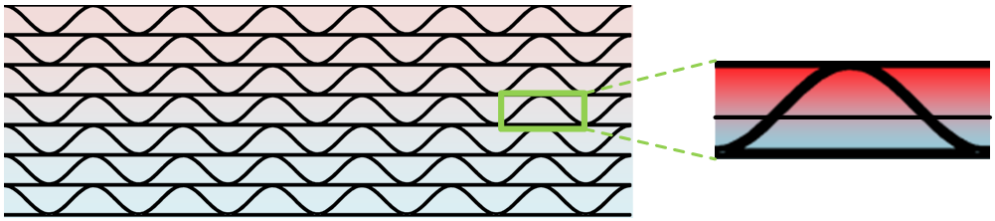

Figure 1. Corrugated foil monolith (prismatic) and thermal gradient.

In rectangular space, thermal gradients are identical when viewed parallel to the foil sheets, resulting in no directional heat transfer. Heat in metal monoliths only moves perpendicular to the sheets where the gradient varies. Convection heat transfer is the dominant mode in the radial direction as conduction through thin metal foils is minimal. Conduction cannot be neglected however and is included in the model as (R_{mono}). Thermal resistance due to convection ($R_{conv,i}$) and conduction ($R_{cond,i}$) at the walls is given with Equations (4) and (5). Total resistance between cells was modeled using Equation (3). Temperature differentials are small within a cell, making radiative effects insignificant. Because monolith cells are closed to each other, mass transfer and subsequent thermal mixing are also not present. With those considerations, individual corrugated channels were unimportant from a modeling perspective, and were ignored. To still capture radial thermal variation without modeling each cellular channel, the monolith channels were redefined as a series of annular walls and voids, which were assumed to be homogeneous in the angular direction. These voids or gas "parcels" represent all monolith channels between two concentric walls of a fixed radius. Use of this approach reduced the number of parcels needed to effectively model the monolith by several orders of magnitude. Corrugations in the monolith contributed to conductive radial heat transfer and occupied physical volume in the experimental monolith. To minimize error from this annular approximation, the radial conduction and monolith void fraction (θ) were still included in the model to decrease error. Thermal resistance in the radial direction was calculated using the series model approximation developed by Groppi and Tronconi [28] and is given with Equation (6). Each annular cell volume was multiplied by θ to achieve correct mass flow rates and thermal residence times within the model. As both gas phases and solid phases

contribute to heat transfer, corresponding thermal conductivities for a gas (k_i) and solid (k_s) were incorporated into Equations (4)–(6).

$$R_{th,i} = \left(\frac{1}{R_{conv,i-1} + R_{cond,wall} + R_{conv,i}} + \frac{1}{R_{mono,i}} \right)^{-1} \tag{3}$$

$$R_{conv,i} = \frac{D_h}{Nu\, k_i} \tag{4}$$

$$R_{cond,i} = ln\left(\frac{r_i + r_{foil}}{r_i} \right) \frac{1}{2\pi k_s dx} \tag{5}$$

$$R_{mono,i} = \frac{1}{1 - \sqrt{\theta} + \frac{\sqrt{\theta}}{1 - \sqrt{\theta} + \frac{k_i}{k_s}\sqrt{\theta}}} \tag{6}$$

The model's approximation using annular sections was set up to match the geometric features of the experimental monolith. The rolled corrugations of the physical monolith result in a single spiraling wall with no fixed radius, and sinusoidal ducts in-between. This physical difference was approximated in the model using the dimensions of a single sinusoidal cell of the experimental monolith. Known through manufacturer specifications, the experimental monolith cell density of 600 cells per square inch (CPSI) was used to determine the open area of a single cell. Distance between walls of concentric annular sections was assumed equal to the calculated height of cells in the experimental monolith. The sinusoidal cell aspect ratio, $2a/2b$, was physically measured to be approximately 1.0 in the experimental monolith and was used to calculate cell height from known cell area. The hydraulic diameter (D_h), used in dimensionless number calculations, was determined using arbitrary duct calculations reported in Shah [16].

Representative model geometry is shown as face and axial section views in Figure 2. A typical temperature profile is also shown, where heat is moving from the outer monolith section to the inner monolith section. The support mantel connects the two monolith sections and creates thermal resistance between them.

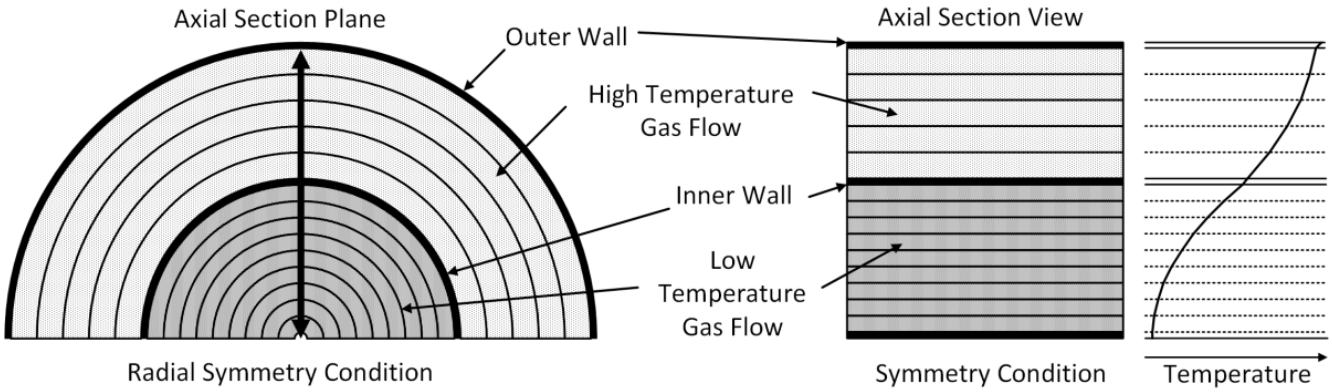

Figure 2. Schematic of monolith cross-section.

Concentric annular sections were modeled with a series of simultaneously solved constant pressure control volumes, with heat exchanged through their shared walls. Heat transfer and adjustment of gas properties all occurred simultaneously in annular sections. Annular sections were also divided along the axial direction into discrete control volumes. Properties from one control volume passed to the next in axial sequence, emulating plug flow in the monolith. By discretizing the control volumes into small enough parcels, the two-dimensional effects in the radial and axial directions were approximated with acceptable accuracy. Increasing the number of axial divisions decreases the modeling error introduced by using discrete parcels with perfect model convergence achieved as

parcels become infinitely small. Useful information can be generated using few parcels, which is desirable for initial qualitative assessment. Parcel count can be refined to required tolerance and can be increased as needed. This allows for rapid design screening and prototype development.

2.2. Heat Exchange Process

A constant Nusselt number (*Nu*) was used to estimate convective heat transfer in the model. As reported by Shah [16], the Nusselt number approaches an asymptotic value as flow becomes fully developed. The value for *Nu* is dependent on the duct geometry alone. For this assumption of constant *Nu* to be valid, it must be shown that the experimental flow entry region is much shorter than the fully developed region. The inverse Graetz number (*Gz*) quantifies this condition. Cornejo et al. [12,13] examined the heat transfer effects within the single cells of a metallic monolith and quantified the developing region *Nu* as a function of *Gz* (Equation (7)).

$$Gz = \frac{D_h}{x} Re\ Pr \tag{7}$$

In these same works, Cornejo et al. compared approaches using averaged and continuously varied fluid properties and found that averaging overestimated *Nu* in the initial developing flow. Overestimation was exaggerated for higher values of the Reynolds number (*Re*). When flow became fully developed, both methods converged, with overall discrepancies due to the relative length of the developing region to the total length. In their study, flow and *Nu* were fully developed when $Gz^{-1} = 5 \times 10^{-1}$ for $50 < Re < 600$. In our work, *Nu* was assumed to be constant. This assumption requires that most of the monolith length be under fully developed conditions. Table 1 reports our experimental ranges of *Re*, the Prandtl number (*Pr*), and Gz^{-1} as calculated at the monolith exit. Minimum reactor-exit Gz^{-1} was found to be one order of magnitude larger than that corresponding to fully developed *Nu* in prior works by Cornejo et al. [12,13]. This implies that at minimum 90% of each experimental flow in our work was fully developed. Assumption of constant *Nu* throughout the length of the monolith will result in minimal modeling error.

Table 1. Dimensionless number ranges in monolith heat exchange experiments.

	Minimum	**Maximum**	**Average**
Re	1.3	40.2	13.3
Pr	0.664	0.744	0.703
Gz^{-1}	5.4	153.2	33.9

Heat transfer between gas parcels was modeled using a thermal resistance network between neighboring parcels. Gas parcels were assumed to be homogeneous with lumped capacitance. Walls between parcels were assumed to be massless, but with finite thickness, which contributes to the overall thermal resistance and void fraction of the monolith assembly. Resistances were calculated in cylindrical coordinates, with convection conditions assessed at the inner and outer diameters of each dividing wall. Figure 3 shows a schematic of this approach between two parcels, with representative temperatures and resistances as modeled. R_1 and R_5 are convective resistances, modeled using a constant *Nu* and gas properties of the parcel. R_2 and R_4 are the thermal conductivities of the coating on the monolith, which was calculated to be 6 microns thick per side of the wall based on loading data provided by the manufacturer. R_3 is the resistance of the monolith foil itself. The monolith foil was modeled using the thermal conductivity of its constituent FeCrAl metal, with a thermal conductivity of 16.8 W/m-K.

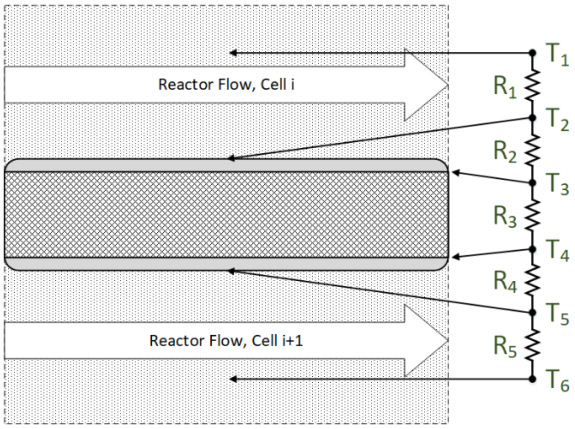

Figure 3. Thermal resistance network used to model heat transfer between reactor cells.

With thermal resistances established in the radial direction between each parcel, heat exchange can be modeled between parcels using a finite difference approach. Figure 4 graphically shows the process, which elaborates on the previously described resistance network to encompass all walls and parcels. For a single axial step, *dx*, the convective heat transfer coefficient was calculated at each wall surface and the conductive contribution from the monolith was also calculated. The two were combined as an apparent heat transfer coefficient and applied at each unique wall surface. Each parcel contained two wall surfaces, with a heat transfer rate assessed at each. To solve the parcels simultaneously, a network of chemically inert constant pressure reactors was created in Cantera. Wall objects in Cantera were installed between each reactor with their respective surface areas and thermal resistances. Using this method, the axial step *dx* was solved in 100 subdivided discrete time-steps to capture the unsteady heat rates and changing temperature differentials. Use of sufficient subdivisions prevented error in discrete solving. Without subdivision, heat transfer rates would be over-represented, and nonsensical temperature changes could result (e.g., inversion of parcel pair temperature differential instead of equalization).

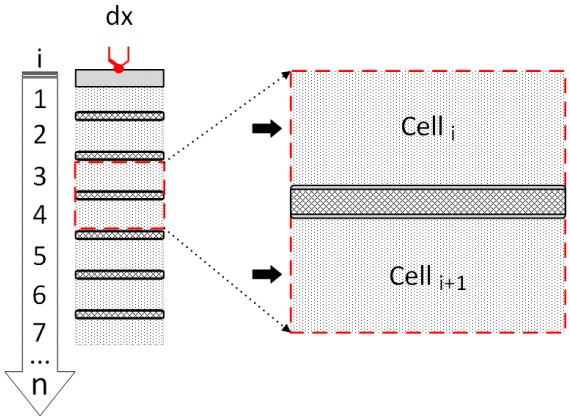

Figure 4. Simultaneous discrete solving of heat transfer between cells in radial direction.

Complete modeling of the heat transfer process consisted of sequential solving of each axial step, from the monolith entrance to exit. After the initial flow and temperature conditions at the inlet to each annular section, subsequent temperature changes were driven entirely by the temperature differential between the wall and the annular parcels. Following each axial step, the properties and flow conditions were passed to the next axial step to undergo the same heat transfer and subsequent property changes. This process is shown graphically in Figure 5 for an arbitrary length of the reactor with time marching forward from left to right. Results from axial section "*i*" were passed to "*i* + 1", where

heat transfer was modeled, and properties were recorded. The process was repeated for "i + 2", and so forth, until the last step, where the final properties were summed on a mass-weighted basis. Properties and temperature values were recorded for every parcel at each axial step, allowing quasi-spatial inspection of thermal behavior. The integral heat transfer coefficient (h_{int}) and heat exchanger effectiveness (ε_{HX}), defined in Equations (8) and (9), were calculated based on the average enthalpy difference achieved between the entrance and exit and the log mean temperature difference ($LMTD$) of the fluid and the monolith mantel wall.

$$h_{int} \equiv \frac{\dot{Q}}{(LMTD)A_{monolith}} \tag{8}$$

$$\varepsilon_{HX} \equiv \frac{\dot{Q}}{\dot{Q}_{max}} \tag{9}$$

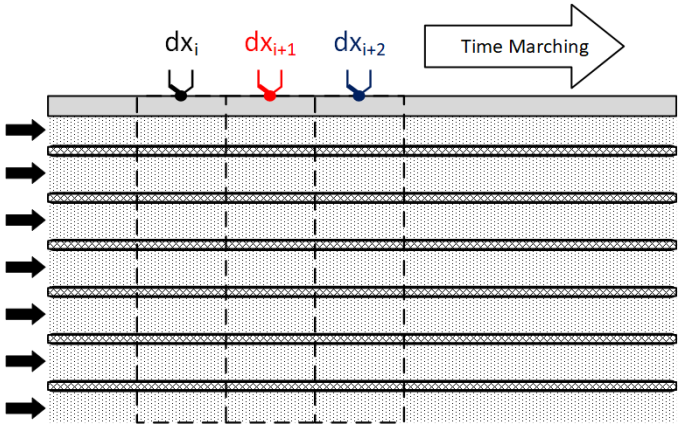

Figure 5. Sequential solution along axis of heat exchange model.

Experimentally, the mantel wall temperature was measured at five equidistant points to determine the effective "skin" temperature. This temperature can be used to reduce model complexity as the outer monolith heat transfer contribution can be assumed via surface temperature. Since the mantel's axial skin temperature profile must be continuous experimentally, the five discrete measurements on the mantel surface were fit to a continuous function. A 3rd order polynomial provided the best fit over all experimental measurements. For modeling each axial subdivision, this continuous function was sampled at discrete axial coordinates and used to calculate heat transfer with a constant wall temperature. Figure 6 illustrates the process of fitting the skin temperature alongside the cross-section view of the endothermic monolith. For a discrete axial section, dx, the effective skin temperature is assumed to be constant. Heat transfer calculations then proceed for all annular cells at dx with the mantel skin acting as an infinite thermal reservoir. This process repeats until the final axial division is calculated.

Model output parameters of interest were the average outlet temperature and the thermal gradients along the axial and radial directions of the monolith. Mass flow per unit volume was assumed to be uniform and constant. Flow velocity and residence time varied due to changing gas properties and were accounted for in the constant pressure reactor network approach. The uniform mass flow rate per unit volume was used to form a weighted average of temperature and enthalpy at the reactor exit. Initial conditions to the model were varied to represent each experimentally tested point. Modeled temperature gradients and heat transfer rates of each condition were recorded for a later experimental comparison and analysis.

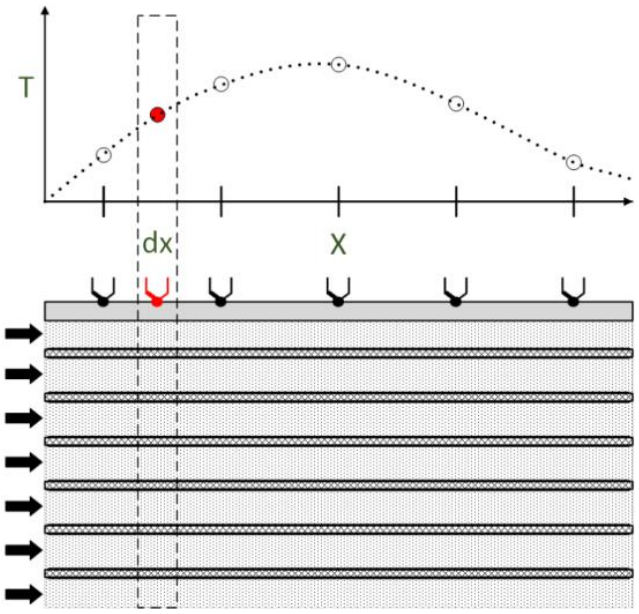

Figure 6. Full-scale discretized modeling of metallic monolith heat transfer along the reactor axis.

2.3. Fluid Properties

Gas properties in the model were continuously updated as temperature changed. Gas parcel temperatures were stored and managed using Cantera gas objects, which also allowed calculation of specific heats, viscosities, and densities at every discrete step for any gas composition. Control volume residence time was calculated using the continuity equation and the density of the gas at any discrete step. Non-dimensional parameters were calculated as well, with Prandtl, Reynolds, and Graetz numbers of particular interest in this work.

2.4. Model Division-Size Convergence

A convergence study was carried out for both model channel divisions, and the discrete time-step subdivisions within each division. For subdivisions, the number was considered converged when heat exchanged across the initial division, where the temperature differential is greatest, changed by less than 0.5% with additional subdivisions. The initial subdivision count started at 10 and increased by 10 until the model converged. The final converged division count was 100 subdivisions. A similar study was used for the axial division count, except the total heat transfer rate in watts was used, and a change threshold of 1% was used. Convergence was achieved at 50 divisions. These division and subdivision counts were then used throughout this study.

3. Experimental Methods

To validate the heat transfer model, the physical construction and flow parameters of concentric metal monoliths were measured under various thermal conditions. The geometry of the structures was first measured. The monoliths were then instrumented with temperature and pressure detection at strategic points. Temperature and flow into the monolith were controlled using a specialized characterization bench. Finally, Design of Experiments was used to decrease the total number of experimental conditions needed to fully characterize the monolith heat transfer behavior.

3.1. Monolith Module Construction

Experimental model calibration was performed using a monolith module consisting of an inner cylindrical monolith and an outer annular monolith. Like the modeled geometry, the two monoliths were brazed to a central mantle to form a seal and decrease contact thermal resistance between the sections. The mantle tube was constructed of 316 stainless

steel pieces and measured 63.5 mm in diameter with a 1.5 mm wall thickness. The outer monolith was rolled to a diameter of 124 mm and fit to a thin stainless sheath of a 127 mm outer diameter. A frontal view with these dimensions is given in Figure 7. The module was operated with heated airflow in the outer annulus and various inert gas flows in the inner cylinder. Temperatures and flow rates to both monoliths were varied using a custom flow bench. Temperatures of the exterior wall of the monolith tube and temperatures of the inlet and outlet monolith flow were measured using K-Type thermocouples. Flowing gas temperatures were selected and managed such that inert species within the inner section were always receiving heat flux from the outer monolith section and never vice versa.

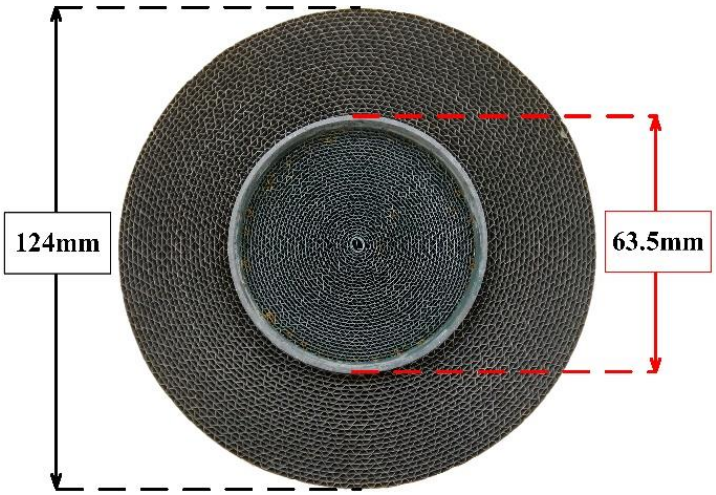

Figure 7. Flow-through view of experimental monolith module with dimensions.

A metal monolith presents a challenging geometry for heat exchange processes. Thermal gradients are generated primarily with convection at corrugation walls. Conduction effects are minor due to the high open areas of the foil monoliths. When monoliths are coupled for heat exchange as shown in Figure 8, heat must first pass through the shared mantle. Flow rates, temperatures, and monolith geometry can be varied to increase this heat exchange, depending on the application. Arrows in the figure highlight heat flow from the monolith annular section towards a cooler cylindrical section. Heat from the annular section is also lost to the ambient environment through the outer-most walls of the monolith. In a practical reactor, the outer walls would typically be insulated to minimize losses and maximize potential recovery.

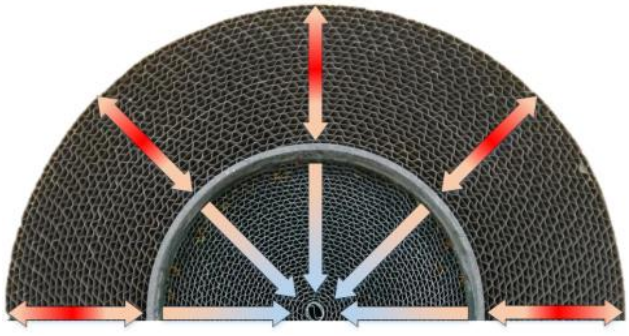

Figure 8. Thermally coupled monolith from Figure 7. The figure graphically depicts radial heat transfer within the annular monolith sections.

3.2. Monolith Module Instrumentation

The supporting mantle provides a boundary for all radial heat transfer to the inner monolith. Therefore, measurement of its temperature was necessary. Efforts were taken

to minimize observer effects on measurement accuracy. Wall surface temperature was measured using five type-K thermocouples (Omega). Probes were inserted through drilled holes from the outer wall of the outer monolith, through the monolith foil layers, to the supporting mantle tube surface. Each wall thermocouple was staggered by 45° to minimize downstream flow effects in the monolith. Drilled holes were countersunk into the surface of the inner monolith wall to a depth of approximately 0.6 mm. Thermocouple tips fit into the countersunk depression produced with drilling, which increased thermal contact with the wall. Figure 9 below shows this strategy, with the temperature-sensing tip of the thermocouple probe at or near the radial depth of the wall's outer surface. The ungrounded tip-sensitive thermocouple was electrically insulated with densely packed magnesium-oxide powder. The thermal conductivity of this packed oxide was like that of the stainless-steel probe body and supporting wall. Placement of the sensing junction near the depth of the mantel wall surface and the similar thermal conductivities of all materials ensured that the measured temperature approached the actual wall surface temperature as accurately as possible.

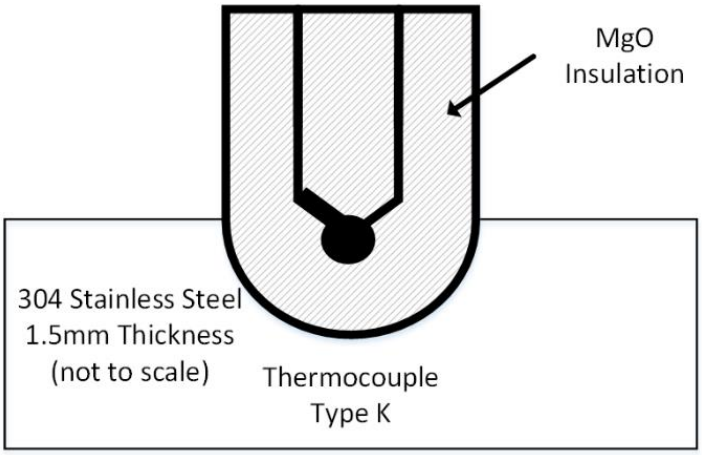

Figure 9. Countersinking strategy for accurate wall temperature measurement.

3.3. Monolith Characterization Apparatus

Experiments were carried out using a custom flow bench equipped with high-flow heating for both inert gases and room air. Configuration of the device is shown in Figure 10. Schematics of the device show flow paths for process gases and the location of heating elements. Inner monolith flow was regulated using a single Sierra Smart-Trak II C100M mass flow controller (MFC), which was factory calibrated for 5 SCFM of ammonia vapor. Gas correction factors (GCF) for thermal mass flow controllers were used to calculate the actual flow of inert species through the MFC. Inert species were regulated to 1 bar gauge and maintained at a room temperature of 20 °C before flowing through the MFC. Flow through the inner monolith was reversible, allowing for co-flow or counterflow modes. Simulated exhaust and reactor outflow were combined downstream of the reactor and removed from the test cell using dedicated building exhaust. Inert species were heated using a Tutco Sureheat 8 kW tube heater (P/N: F074719). Outer monolith airflow was created using a Fuji Electric 2.5 HP Ring Compressor and was heated using four parallel 8 kW Leister LE-5000 heaters. The assembly was capable of producing airflow of up to 58 g per second at temperatures of 625 °C at the monolith inlet. Temperature was varied using built-in temperature controllers within the Leister heaters, and the air flow rate was modulated using a throttle plate upstream of the compressor.

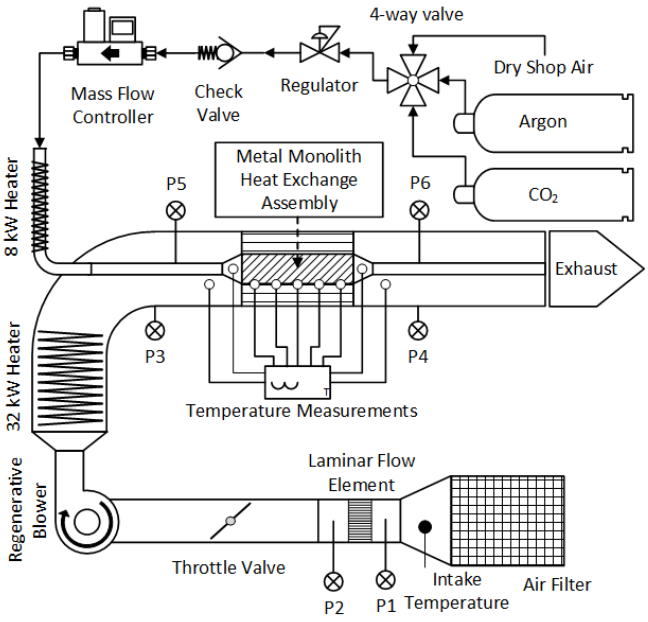

Figure 10. Experimental configuration for inert heat transfer experiments.

3.4. Experimental Procedure

Three different inert species, carbon dioxide (CO_2), argon (Ar), and clean dry air (CDA), were used in the experiments due to their availability and variation in thermal properties. CO_2 and Ar were obtained as compressed pure bottle gases, and CDA was generated on-site using molecular sieves. Variation in the properties of these gases resulted in varied volumetric heat capacities, providing a wider range of conditions for model calibration. Standard gas properties of these species are reported in Table 2.

Table 2. Standard gas properties for heat transfer validation experiments.

		Dry Air	**Argon**	**CO_2**
Density	g/L	1.293	1.782	1.964
Specific Heat	J/g-k	1.004	0.520	0.843
GCF	[-]	1.00	1.39	0.70

Flowrates, pressure, and temperature measurements from the characterization bench were logged continuously using an in-house LabVIEW data acquisition method at a rate of 1 Hz. Baseline experimental conditions were set using the characterization bench and allowed to stabilize before measurement. Average temperature and pressure measurements were later used as model inputs, against which the resulting model output could be calibrated.

3.5. Surface Response Methodology

A surface response methodology (SRM) was employed to reduce the number of input test conditions required to achieve understanding of the overall monolith design space. A Box–Behnken design experimental matrix was created using the JMP 15 ™ statistical software package [29] to minimize the number of independent test conditions. The SRM design is reported in Supplementary Information, Table S1 and was repeated for each gas independently. The four independent variables tested were the two inlet temperatures and two gas flow rates for the inner and outer monolith sections. Due to contact between the inert gas flow and the heated air flowing through the outer monolith section, inert gas temperature to the inner section experienced a minimum temperature that varied. Inner monolith inlet temperature was thus varied using a floating temperature zero, which corresponded to the minimum achievable inlet temperature. This floating

zero was reassessed for each outer monolith flow rate and was established at the highest air temperature allowed at that flow rate. Using this floating zero, inner monolith inlet temperatures were tested at 0 °C, 50 °C, and 100 °C above the baseline. SRM test conditions were ordered based on ascending temperatures to minimize stabilization wait time and were sampled for 300 s to acquire a stable measurement.

3.6. Experimental Uncertainty Analysis

Experimental measurement uncertainty was calculated using one standard deviation of the measurement for each steady-state condition. Experimental uncertainty in each calculated value was determined using the standard error propagation method. Calculation uncertainty across repeated test conditions was estimated using the steady-state uncertainty calculation combined with the weighted repeatability error arising from each experimental replicate. Modeling uncertainty, where applicable, was calculated using the numerical sequential perturbation method [30]. Error bars on figures correspond to the root mean square value of one standard deviation from the mean of the total samples taken for that test condition.

4. Results and Discussion

To calibrate the heat transfer model, a constant fully developed Nusselt number (*Nu*) was sought. A single *Nu* was found by minimizing root mean square error (RMSE) across the entire SRM experimental dataset. Once a satisfactory *Nu* was established, the calibrated model was then subjected to a new full-factorial study where geometric parameters of the modeled monolith were varied. Effects of various construction and flow parameters were analyzed, and their outcomes fit using simple linear equations to provide useful trends in how geometry affects heat exchange.

A total of 420 unique experimental test conditions were measured under the conditions designated in the SRM, with three replicates for each gas and flow orientation. Range-finding and experimental preparations yielded two additional complete replicates for the co-flow air condition, and the data were included with the three original replicates to create five distinct measurements of each condition. Runtime to model all 420 conditions using baseline model divisions (100) and subdivisions (100) was 3528.4 s or 8.4 s per condition. A stock clock rate Intel i7 5820K was used to run the model on a single thread with no added acceleration. The original goal of computationally cheap and accurate monolith modeling was thus proven, and the results are discussed in following passages.

4.1. Determination of Optimal Nusselt Number

With constant geometry, the value of *Nu* should remain constant across different gases and flow orientations. As it is also critical to convective heat transfer, it is necessary to determine to model the heat exchange process. A binary search algorithm was used to determine an optimized *Nu* value from the data. In his examination of arbitrary ducts, Shah [16] established bounds of $2.0 \leq Nu \leq 4.0$ for sinusoidal profiles. These bounds were used to constrain the search algorithm. The modeled reactor bulk outlet temperature was used to determine model validity, with the inherent stratification of the model weighted with each channel's relative mass flow at the outlet to determine a mean value. The RMSE in the model outlet temperature was used as the algorithm loss function and was minimized using $Nu = 3.12$ for the entire dataset. This value is within the range of values established by Shah and Cornejo et al. [12,13]. Fitting the model to experimental data using this value resulted in a near-linear fit. Figure 11 shows these data as a scatter plot, with distinction between the flow pattern of the experiment and the inert gas used. Modeling trends show slight overprediction of the outlet temperature for co-flow and underprediction in counterflow. The slopes of both flow patterns follow that of the dashed prediction line, indicating that the error between the model and measurement is offset by a fixed value. Factors such as measurement uncertainty and day-to-day variability could induce such error. The thermocouples used to measure inlet and outlet temperatures are

reversed between co- and counterflow conditions. Thermocouple aging, drift, and the asymmetrical insulation and flow characteristics between the two ends of the reactor could induce additional thermal effects, which the model does not capture. The co-flow outlet thermocouple is in indirect thermal communication with the cooled exhaust outlet, while the counterflow outlet thermocouple is in indirect thermal communication with the exhaust inlet. Minor radiative heat transfer from the heated inlet/outlet tubes would influence the thermocouple measurement in these cases, increasing the counterflow temperature measurement and decreasing the co-flow measurement under otherwise identical conditions. This is evident in the consistent overprediction and underprediction of the model, which increases at higher temperatures.

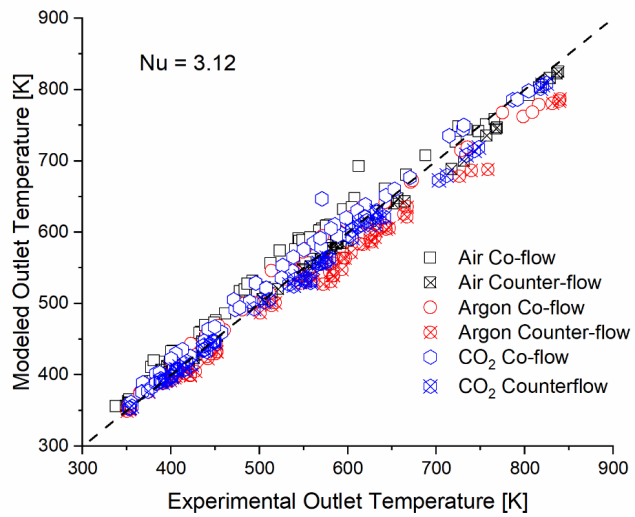

Figure 11. Linear scatter plot of modeled outlet temperature vs. experimental measurements.

The minimized root mean square error was determined to be 20.16 K, which is acceptable considering the high flow rates and temperatures of the heat exchange assembly. For the case of reaction modeling, a change in temperature of 20 K would not change the reaction yield or activity under high throughput conditions. As shown in Figure 12, the error was centered around an average of 0 K and the relative modeling error (%) was generally 5% or less. This is acceptable from a heat transfer standpoint, considering the high-speed solution offered with this approach. After design screening, further accuracy can be obtained through more accurate modeling methods like CFD.

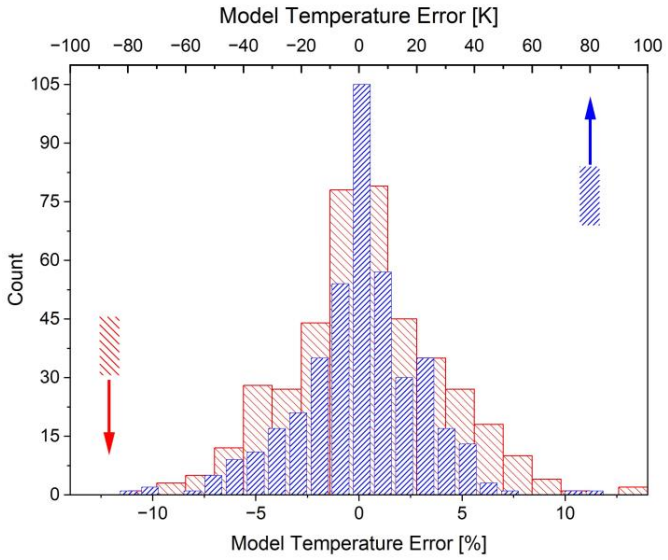

Figure 12. Histogram of modeling residuals in predicted outlet temperature.

4.2. Parametric Study

After *Nu* calibration, the geometry of the modeled monolith was varied in a full-factorial analysis focused on the heat exchange effectiveness and integral heat transfer rate as responses. This model examined just the cylindrical inner monolith and assumed a constant elevated wall temperature to drive the heat exchange process. Input variables included the cell density of the monolith (CPSI), the flow rate through the monolith, the wall temperature (T_{wall}), and the aspect ratio of the monolith (α). The monolith aspect ratio is defined with Equation (10). The flow rate was reported as a gas-hourly space velocity (GHSV), which is a typical metric for catalyst systems. Response data from the full factorial model were processed in JMP 15 ™ to determine the relationships between the four independent variables on the thermal responses. The simple model generated using JMP for both dependent variables is shown in the scatter plots of Figure 13. Perfect linear agreement is plotted using a solid red line. Linear regression of a model output is an unconventional but useful approach in this analysis. By performing a regression, a simple and relatively accurate relationship between each variable to the response can be obtained. Fit Equations (11) and (12) are formulated such that each independent variable is normalized to vary from +1 to −1, making the slopes of all variables directly comparable. The relative importance of each variable can thus be discerned with the magnitude of its slope.

$$\alpha \equiv \frac{L}{D} \tag{10}$$

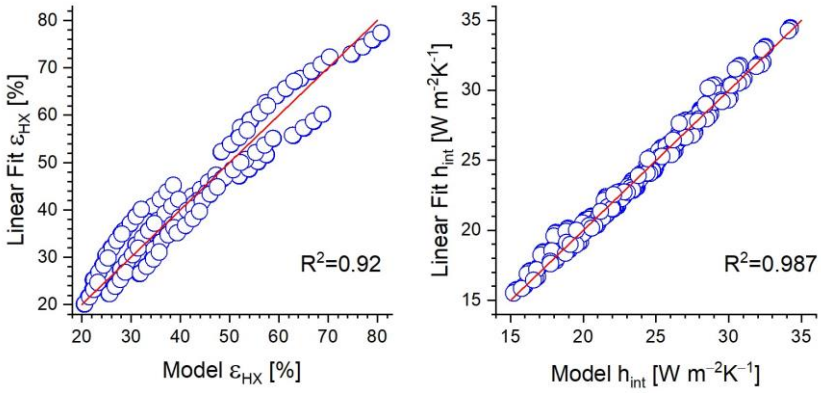

Figure 13. Simple linear fit models for heat exchange effectiveness and integral heat exchange coefficients.

Heat exchanger effectiveness defined earlier with Equation (9) was fit using multiple linear regression, yielding Equation (11). Minimization of the sample RMSE was used to determine best fit. Effectiveness was found to vary as a function of the four independent variables. RMSE was 4.07%, with an R^2 of 0.92. Most important to the heat exchange effectiveness is an aspect ratio, α. Monolith geometries with smaller diameters and longer channels result in higher heat exchange effectiveness. GHSV has the second-highest impact, with low velocities leading to the highest efficiencies. Physically, increasing flow to a heat exchanger will decrease efficiency under normal circumstances due to decreased residence time. This assumes that the flow conditions within the heat exchanger do not drastically change the convective heat transfer through turbulent transition or other means. Wall temperature does not strongly affect the heat transfer efficiency due to the temperature differential being captured in the heat exchange effectiveness term. Minor impact results from an increased thermal differential near the outer radii of the cylinder. Due to radial conduction, which scales with the natural log of the radial distance, the apparent thermal resistance along the radius increases as the radial position approaches zero. The higher absolute temperature differential increases the overall penetration of heat due to the more complete heating of these outer radial positions. Cell density was shown to have almost no effect on the heat exchange effectiveness. In the three examined densities, flow was wholly laminar and modeled as such with the terminal Nusselt number from experimental fitting. Without physical modeling of the wall structures, the effects of catalyst wash coating, or capturing minute variation in individual cells of the monolith, it is impossible to determine if cell density more strongly affects heat exchange effectiveness or plays no role whatsoever. From this regression, it is clear, however, that its effect is minor.

$$\varepsilon_{HX} = 0.487 + \left(0.0225\frac{(T_{wall}-723.15)}{150}\right) - \left(0.1028\frac{(GHSV-12000)}{600}\right) + \left(0.1621\frac{(\alpha-425)}{3.75}\right) + \left(0.000340\frac{(CPSI-750)}{450}\right) \quad (11)$$

Values of h_{int} were also modeled in JMP 15 ™ using a simple linear fit to analyze the individual contributions of each independent variable to the overall system. The fit is reported in Equation (12), with similar scaling coefficients to indicate relative importance to the final value of h_{int}. The best fit for the integral heat transfer coefficient was found as presented, with an R^2 of 0.98743 and an RMSE 0f 0.481 W m^{-2}K^{-1}. Like the heat exchange effectiveness, the cell density was relatively unimportant to the overall heat exchange rate. This makes sense, considering that some of the physical phenomena, which would change experimentally with cell density, such as the void fraction and conduction, were held constant in the model. These values were not varied as inputs to the model as they depend on the foil thickness chosen during monolith construction. As this variable could vary widely based on engineering requirements, the added complexity and expense of its inclusion would not yield comparable information useful for this study. Aspect ratio and

temperature both show a similar scale of importance in affecting h_{int}. As shown previously by Boger and Heibel [17], higher wall temperatures lead to higher log-mean temperature differential (LMTD) values in a monolith, which, in turn, create higher integral heat transfer coefficients. The same effect is shown in this modeling. Integral heat transfer rates are 1–2 orders of magnitude lower than those measured experimentally by Boger and Heibel. This is due to the larger diameter monolith used in this study, the lower-conductivity monolith material, and the convective condition at the monolith shell. This study used heated gas at the shell, whereas the previous study used circulating liquid water, which would provide at least an order of magnitude larger convective rate at the surface.

$$h_{int} = 24.987 + \left(2.0404\frac{(T_{wall}-723.15)}{150}\right) + \left(5.0811\frac{(GHSV-12000)}{600}\right) + \left(2.2401\frac{(\alpha-425)}{3.75}\right) - \left(0.1146\frac{(CPSI-750)}{450}\right) \quad (12)$$

Two considerations must still be made regarding cell density. The pressure drop across the assembly is affected by cell density regardless of heat transfer effects. Higher cell densities have lower open cross-sectional areas, leading to higher restrictions. Higher cell densities also have higher surface area to volume ratios, leading to higher wash-coat loading and greater reactor intensification. The finding that cell density does not affect heat exchange effectiveness makes the design process simpler. The trade-off becomes one of catalytic performance required versus wash-coating cost under constant heat exchange capabilities.

Modeled values for h_{int} were already shown to vary as a function of GHSV, the aspect ratio, and the initial temperature differential (ΔT_{init}). This effect is best illustrated using continuous contour plots for various temperature differentials. Figure 14 shows a series of these contour plots generated from the model, which further illustrates this relationship. Increasing ΔT_{init} consistently increases h_{int} regardless of other input parameters. At aspect ratios below unity, the slope of contours shows a decreasing trend. The lower limit of the aspect ratio, which approaches zero, implies an infinitely flat disc of an infinite diameter. In this case, it would be expected that thermal resistance would go to infinity. It follows that these curves will rapidly collapse upon each other as the aspect ratio approaches zero. It is intuitive that a flat disc heated from the rim is not conducive to heat transfer. Moving in the other direction, towards high aspect ratios, it is shown that the contour slopes become flat, reflecting the linear fit shown earlier. An increased aspect ratio increases the surface area to volume ratio, which decreases the thermal path length from the heated outer surface to the internal gases, thereby increasing the overall heat transfer rate. For a cylinder of constant volume whose geometry varies with the aspect ratio, the surface area to volume ratio is given with Equation (13). Aspect ratio in the numerator confirms this observation. The physical significance of the heat exchange coefficient is an indication of overall resistance to heat flow.

$$\frac{SA}{V} = \frac{4\sqrt[3]{\pi a}}{\sqrt[3]{4V}} \quad (13)$$

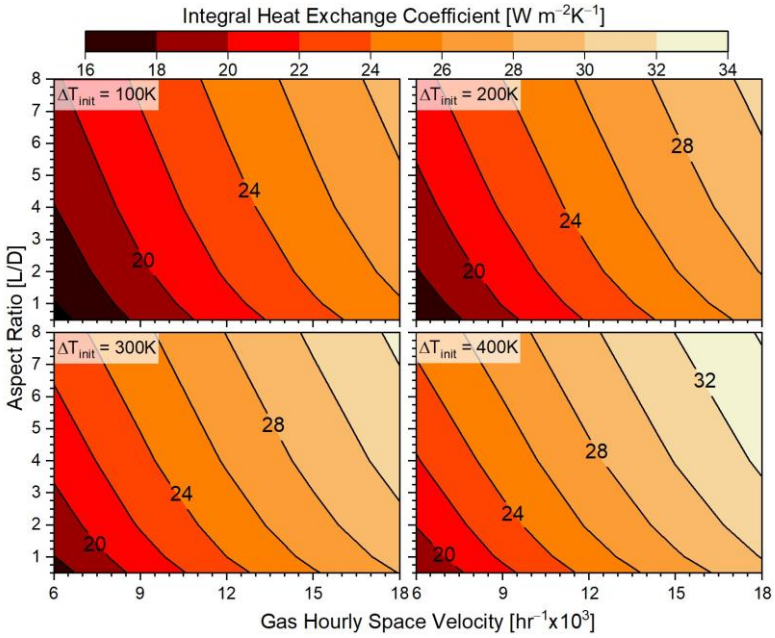

Figure 14. Modeled integral heat transfer coefficient at the wall of the reactor for varied GHSV and aspect ratio.

Heat exchanger effectiveness was calculated for the same conditions described above and arranged in four contour plots, as shown in Figure 15. As can be seen, heat exchanger effectiveness varied from 21% to 81% and was highly dependent on input conditions. Low GHSV resulted in higher efficiency, which makes intuitive sense as gas was exposed to the heated wall for a longer duration of time. Increasing the aspect ratio was also shown to increase efficiency. As with integral heat transfer rates, the surface area to volume ratio increases with the aspect ratio and increases exposure of monolith gases to the heated wall. The diameter of the monolith decreases as well, leading to lower thermal resistance between the bulk of monolith gas and the surrounding wall. A larger initial temperature differential showed a marginal increase in efficiency, which was more pronounced when the aspect ratio was large. Because a low aspect ratio creates such a large thermal resistance between the wall and the bulk of flowing gases, changing the initial temperature differential here showed little effect and efficiency was low in all cases. The opposite occurs in high-aspect-ratio conditions, where a higher temperature differential drives greater heat exchange rates, leading to the bulk of gases nearly equalizing with wall temperature via the outlet of the monolith.

To summarize, while parametric investigation confirmed an intuitive relation between thermal inputs, flow rates, and their effect on heat exchange outcomes, it also revealed surprising relationships between some of the parameters. Cell density showed little effect on thermal performance of theoretical monoliths, while a varying aspect ratio showed a significant effect due to the inherent change in the surface area to volume ratios. This means that heat exchange effectiveness would be maximized at minimum GHSV and at high aspect ratios, whereas heat exchange rates are maximized with GHSV, the temperature differential, and the aspect ratio. Because of the competing effect of the gas flow rate on the two parameters, a compromise in the design must be made. For example, in a steam reformer, the monolith design could be optimized to provide high absolute conversion at a low flow, high molar conversion at a high flow, or some middle point between those two. The optimum operation condition depends on the end use, but any of these cases can be targeted through this modeling approach.

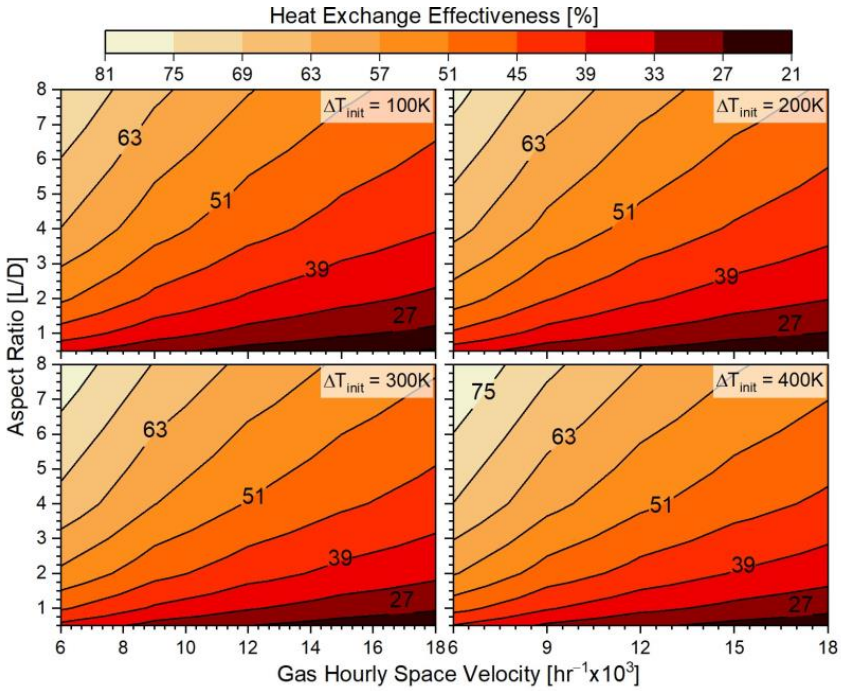

Figure 15. Modeled heat exchange effectiveness at the wall of the reactor for varied GHSV and aspect ratio.

5. Conclusions

A computationally inexpensive, yet sufficiently accurate, heat transfer model was developed for inter-monolith heat transfer in a concentric configuration using a control volume approach and discretized solving. The model assumed radial symmetry and resolved the monolith along axial and radial dimensions. The model was validated using an experimental monolith assembly as a heat exchanger between heated air and inert gases. Heat exchange rates were calibrated by solving for a fully developed Nusselt number, which was determined through a binary seek algorithm. This algorithm was used to fit the model to experimentally measured values. Best fit was determined with minimization of the RMSE between the predicted outlet temperature of the model and the observed outlet temperature for all experiments using a single value for *Nu*. The *Nu* value found through this method was 3.12, which was within the range reported in prior literature and reasonable for generic internal flow.

After Nusselt number calibration, the geometry of the modeled monolith was varied in a full-factorial analysis focused on the integral heat transfer rate and heat exchange effectiveness responses. Relative effects of all input criteria were analyzed using JMP 15 ™ software and multiple linear regression of the model output was used to simply describe the individual effects of each on the response. Aspect ratio and GHSV were the most important factors in the net response. The initial temperature differential showed a small impact on heat exchanger effectiveness, with little variation between contour plots. However, the initial temperature differential was shown to be nearly as significant as the aspect ratio regarding the integral heat transfer rate, generating a significant shift in the contour plot's upper bounds. Cell density of the monolith was shown to be unimportant for both output criteria.

Contour plots were generated using regression parameters to show a continuous response using the three significant input conditions. Optimum heat exchange efficiencies were achieved by minimizing gas flow rate GHSV and maximizing the aspect ratio and initial temperature differential. In contrast, optimum heat transfer rates occurred by maximizing gas flow rate GHSV, with all else held constant. Using a baseline condition, α = 1.0 and GHSV = 6000, this corresponded to a heat exchange efficiency increase of 43.2%, and a heat transfer increase of 44.8% at respective optimum conditions. These findings

indicated that for a given reactor design, one of these two operation modes must be selected to maximize performance. Maximum conversion will occur where temperatures are the highest, under the high heat exchange condition. Maximum heat recovery will occur in the maximum heat exchange coefficient condition. While one mode or the other will offer a greater benefit to a specific system, increasing the aspect ratio of monoliths was shown to improve heat transfer rates and efficiency regardless of the desired operation mode.

The model presented here easily incorporates changes in monolith geometry, foil material, and process gases, making it well suited for design screening or algorithmic optimization of round catalyst prototypes. While only one geometry was experimentally examined, the full factorial modeling approach showed that rapid screening of monolith parameters reveals immediate design improvements. A future work could further increase accuracy and model robustness through incorporating radiation modeling or mass transfer effects. Nevertheless, the accuracy shown using basic heat transfer and conservation laws is sufficient for early design stage investigation. The modeling procedure of this current work is recommended for identification of promising geometries and flow conditions, which can be later examined thoroughly in computationally expensive CFD models or physical prototype construction.

Supplementary Materials: The following supporting information can be downloaded at: https://www.mdpi.com/article/10.3390/thermo3040031/s1, Table S1: Box–Behnken Response Surface Method for monolith heat transfer study.

Author Contributions: Methodology, all authors; formal analysis and investigation, S.P.K.; resources, all authors; writing—original draft preparation, S.P.K.; writing—review and editing, all authors; project administration and funding acquisition, W.F.N. All authors have read and agreed to the published version of the manuscript.

Funding: The work presented in this manuscript was partially funded by the Legislative Citizen Commission on Minnesota Resources under the Minnesota Legislature 2016 Environment and Natural Resources Trust Fund (ENRTF), Chp. 186, Sec. 2, Subd. 07c. Seamus Kane would also like to acknowledge the financial support provided by the University of Minnesota Institute on the Environment (IonE) through its Renewable Energy Commercialization Fellowship.

Data Availability Statement: Data are contained within the article and Supplementary Material.

Conflicts of Interest: The authors declare no conflict of interest.

Nomenclature

The following nomenclature is used in this manuscript:

$A_{monolith}$	Monolith Shared Interfacial Wall Area, m^2
CFD	Computational Fluid Dynamics
CPSI	Cell Density, Cells per Square Inch, $\#/in^2$
D	Monolith Diameter, m
Dh	Hydraulic Diameter, m
GCF	Gas Correction Factor
GHSV	Gas Hourly Space Velocity, hr^{-1}
Gz	Graetz Number
LMTD	Log-Mean Temperature Differential
MFC	Mass Flow Controller
Nu	Nusselt Number
Pr	Prandtl Number
Q	Heat Transfer Rate, W
Q_{max}	Maximum Heat Transfer Rate, W
R_{cond}	Thermal Resistance due to Conduction between Gas Parcels
R_{conv}	Thermal Resistance due to Convection

R_{mono}	Independent Thermal Resistance due to Monolith Solid Conduction
R_{th}	Thermal Resistance
Re	Reynolds Number
RMSE	Root Mean Square Error
SA	Surface Area, m^2
SCFM	Standard Cubic Feet per Minute
SRM	Surface Response Methodology
T_{init}	Initial Temperature, K or °C
T_{wall}	Monolith Wall Temperature, K or °C
V	Volume, m^3
h_{int}	Integral Heat Transfer Coefficient, W/m^2-K
k_i	Gas Thermal Conductivity of Parcel i, W/m-K
k_s	Solid Thermal Conductivity, W/m-K
r_i	Radial Position of Monolith Wall, m
r_{foil}	$r_i + t_{foil}$, m
t_{foil}	Foil Thickness, m
x	Monolith Axial Position, m
α	Monolith Aspect Ratio, L/D
ΔT_{init}	Initial Temperature Differential, K or °C
ε_{HX}	Heat Exchanger Effectiveness
θ	Monolith Void Fraction

References

1. Heck, R.M.; Farrauto, R.J. Automobile Exhaust Catalysts. *Appl. Catal. A Gen.* **2001**, *221*, 443–457. [CrossRef]
2. Farrauto, R.J.; Heck, R.M. Catalytic Converters: State of the Art and Perspectives. *Catal. Today* **1999**, *51*, 351–360. [CrossRef]
3. Avila, P.; Montes, M.; Miró, E.E. Monolithic Reactors for Environmental Applications: A Review on Preparation Technologies. *Chem. Eng. J.* **2005**, *109*, 11–36. [CrossRef]
4. Nijhuis, T.A.; Beers, A.E.W.; Vergunst, T.; Hoek, I.; Kapteijn, F.; Moulijn, J.A. Preparation of Monolithic Catalysts. *Catal. Rev. Sci. Eng.* **2001**, *43*, 345–380. [CrossRef]
5. Tomašić, V.; Jović, F. State-of-the-Art in the Monolithic Catalysts/Reactors. *Appl. Catal. A Gen.* **2006**, *311*, 112–121. [CrossRef]
6. Govender, S.; Friedrich, H.B. Monoliths: A Review of the Basics, Preparation Methods and Their Relevance to Oxidation. *Catalysts* **2017**, *7*, 62. [CrossRef]
7. Cybulski, A.; Moulin, J. Monoliths in Heterogeneous Catalysis. *Catal. Rev.* **1994**, *36*, 179–270. [CrossRef]
8. Ekström, F.; Andersson, B. Pressure Drop of Monolithic Catalytic Converters Experiments and Modeling. *SAE Tech. Pap.* **2002**, *111*, 425–433. [CrossRef]
9. Tronconi, E.; Groppi, G.; Boger, T.; Heibel, A. Monolithic Catalysts with "high Conductivity" Honeycomb Supports for Gas/Solid Exothermic Reactions: Characterization of the Heat-Transfer Properties. *Chem. Eng. Sci.* **2004**, *59*, 4941–4949. [CrossRef]
10. Maus, W.U.S. Metal Foil with through Openings and Honeycomb. Body. Patent 6,316,121, 13 November 2001.
11. Cornelison, I.R.C.; Retallick, W.B.; Chester, W.U.S. Process for Making Metal Substrate Catalytic Converter. Cores. Patent 4,711,009, 8 December 1987.
12. Cornejo, I.; Nikrityuk, P.; Hayes, R.E. Improved Nu Number Correlations for Gas Flow in Monolith Reactors Using Temperature-Dependent Fluid Properties. *Int. J. Therm. Sci.* **2020**, *155*, 106419. [CrossRef]
13. Cornejo, I.; Nikrityuk, P.; Hayes, R.E. Heat and Mass Transfer inside of a Monolith Honeycomb: From Channel to Full Size Reactor Scale. *Catal. Today* **2022**, *383*, 110–122. [CrossRef]
14. Hayes, R.E.; Fadic, A.; Mmbaga, J.; Najafi, A. CFD Modelling of the Automotive Catalytic Converter. *Catal. Today* **2012**, *188*, 94–105. [CrossRef]
15. Sadeghi, F.; Tirandazi, B.; Khalili-Garakani, A.; Nasseri, S.; Nabizadeh Nodehi, R.; Mostoufi, N. Investigating the Effect of Channel Geometry on Selective Catalytic Reduction of NOx in Monolith Reactors. *Chem. Eng. Res. Des.* **2017**, *118*, 21–30. [CrossRef]
16. Shah, R.K. Laminar Flow Friction and Forced Convection Heat Transfer in Ducts of Arbitrary Geometry. *Int. J. Heat. Mass. Transf.* **1975**, *18*, 849–862. [CrossRef]
17. Boger, T.; Heibel, A.K. Heat Transfer in Conductive Monolith Structures. *Chem. Eng. Sci.* **2005**, *60*, 1823–1835. [CrossRef]
18. Roh, H.S.; Lee, D.K.; Koo, K.Y.; Jung, U.H.; Yoon, W.L. Natural Gas Steam Reforming for Hydrogen Production over Metal Monolith Catalyst with Efficient Heat-Transfer. *Int. J. Hydrogen Energy* **2010**, *35*, 1613–1619. [CrossRef]
19. Cornejo, I.; Garreton, G.; Hayes, R.E. On the Use of Dual Cell Density Monoliths. *Catalysts* **2021**, *11*, 1075. [CrossRef]
20. Reinao, C.; Cornejo, I. A Model for the Flow Distribution in Dual Cell Density Monoliths. *Processes* **2023**, *11*, 827. [CrossRef]
21. Cherif, A.; Lee, J.S.; Nebbali, R.; Lee, C.J. Novel Design and Multi-Objective Optimization of Autothermal Steam Methane Reformer to Enhance Hydrogen Production and Thermal Matching. *Appl. Therm. Eng.* **2022**, *217*, 119140. [CrossRef]

22. Tonkovich, A.Y.; Perry, S.; Wang, Y.; Qiu, D.; Laplante, T.; Rogers, W.A. MicroChannel Process Technology for Compact Methane Steam Reforming. *Chem. Eng. Sci.* **2004**, *59*, 4819–4824. [CrossRef]
23. Kane, S.P.; Northrop, W.F. Thermochemical Recuperation to Enable Efficient Ammonia-Diesel Dual-Fuel Combustion in a Compression Ignition Engine. *Energies* **2021**, *14*, 7540. [CrossRef]
24. Sánchez, D.; Chacartegui, R.; Muñoz, J.M.; Muñoz, A.; Sánchez, T. Performance Analysis of a Heavy Duty Combined Cycle Power Plant Burning Various Syngas Fuels. *Int. J. Hydrogen Energy* **2010**, *35*, 337–345. [CrossRef]
25. Ryu, J.H.; Lee, K.Y.; La, H.; Kim, H.J.; Yang, J., II.; Jung, H. Ni Catalyst Wash-Coated on Metal Monolith with Enhanced Heat-Transfer Capability for Steam Reforming. *J. Power Source* **2007**, *171*, 499–505. [CrossRef]
26. Song, T.W.; Sohn, J.L.; Kim, J.H.; Kim, T.S.; Ro, S.T.; Suzuki, K. Performance Analysis of a Tubular Solid Oxide Fuel Cell/Micro Gas Turbine Hybrid Power System Based on a Quasi-Two Dimensional Model. *J. Power Source* **2005**, *142*, 30–42. [CrossRef]
27. Almeida Pazmiño, G.A.; Jung, S. General Dynamic Modeling of Monolith Catalytic Reactors: Microkinetics of Dimethyl Ether Oxidation on Pt/ZSM-5 Catalyst. *Energy Convers. Manag.* **2019**, *192*, 269–281. [CrossRef]
28. Groppi, G.; Tronconi, E. Continuous vs. Discrete Models of Nonadiabatic Monolith Catalysts. *AIChE J.* **1996**, *42*, 2382–2387. [CrossRef]
29. *JMP*®, version 15; SAS Institute Inc.: Cary, NC, USA, 1989–2023.
30. Figliola, R.S.; Beasley, D.E. *Theory and Design for Mechanical Measurements*; Wiley: Hoboken, NJ, USA, 2011; p. 585.